Science Advances
AAAS

Supplementary Materials for

Shear Shock Waves Mediate Haptic Holography via Focused Ultrasound

Gregory Reardon *et al.*

Corresponding author: Yon Visell, yonvisell@ucsb.edu

Sci. Adv. **9**, eadf2037 (2023)
DOI: 10.1126/sciadv.adf2037

The PDF file includes:

Other Supplementary Material for this manuscript includes the following:

Supplementary Text

Acoustic Radiation Pressure

While ultrasound frequency vibrations cannot be felt by the skin, a nonlinear physical phenomenon, acoustic radiation pressure, causes incident ultrasound to impart low-frequency forces to the skin, eliciting shear wave oscillations. Here, we briefly summarize this physical process, which is essential to ultrasound-based haptic feedback.

The Langevin radiation pressure exerted on a solid body with surface S in an acoustic field yields a resultant force given by

$$\mathbf{F}_L = \left\langle \iint_S dS\, \sigma \cdot \mathbf{n}(t) \right\rangle \tag{1}$$

where σ is the stress tensor, and $\mathbf{n}$ the normal direction. These quantities can vary in time, and the angular brackets denote time-averages over an integer number of oscillation periods. The stress tensor is given by $\sigma = -p\mathbf{I} + \sigma'$, where $\mathbf{I}$ is the unit tensor and σ' the viscous stress tensor. One may equivalently replace the integral in Eq. 1 by an integral over an arbitrary surface, S', that encloses the obstacle

$$\mathbf{F}_L = \left\langle \iint_{S'} dS' [\sigma - \rho \mathbf{u} \otimes \mathbf{u}] \cdot \mathbf{n} \right\rangle \tag{2}$$

where the second term on the right-hand side is the momentum flux tensor and $\mathbf{n}$ is the outward surface normal of the fixed control surface (*34, 35*).

An expression for the time-averaged pressure field may be obtained using the Navier-Stokes equation for an inviscid fluid

$$\rho \partial_t \mathbf{u} = -\nabla p - \rho(\mathbf{u} \cdot \nabla)\mathbf{u} \tag{3}$$

where $\mathbf{u}$, p, and ρ are the velocity, pressure, and density fields, respectively. In a perturbation

analysis expansion, the field quantities can be expressed up to second order as

$$\begin{aligned} \rho &= \rho_0 + \rho_1 + \rho_2 \\ p &= p_0 + p_1 + p_2 \\ \mathbf{u} &= \mathbf{u}_1 + \mathbf{u}_2, \end{aligned} \tag{4}$$

with subscripts 0, 1, 2 representing the base quantity and first-order and second-order perturbations of the fields, respectively. Substituting these into Eq. 3 yields first- and second-order perturbations of the Navier-Stokes equation (*38*)

$$\rho_0 \partial_t \mathbf{u}_1 = -\nabla p_1 \tag{5}$$

$$\rho_0 \partial_t \mathbf{v}_2 + \rho_1 \partial_t \mathbf{u}_1 = -\nabla p_2 - \rho_0 (\mathbf{u}_1 \cdot \nabla)\mathbf{u}_1 \tag{6}$$

An air-coupled ultrasound source yields first-order fields each having a time-harmonic dependence, $f(\mathbf{r}, t) = f(\mathbf{r})e^{-i\omega t}$. Upon time averaging, these terms vanish, leaving only second-order terms. Substituting the expression for $\partial_t \mathbf{u}_1$ from Eq. 5 into Eq. 6, and using $p_1 = c_0^2 \rho_1$, one obtains

$$\nabla \langle p_2 \rangle = \frac{1}{\rho_0 c_0^2} \langle p_1 \nabla p_1 \rangle - \rho_0 \langle (\mathbf{u}_1 \cdot \nabla)\mathbf{u}_1 \rangle \tag{7}$$

In air-coupled ultrasound display, it is appropriate to assume irrotational flow conditions. This leads to an expression for the second-order, time-averaged pressure in terms of first-order quantities

$$\langle p_2 \rangle = \frac{1}{2} \kappa_0 \langle p_1^2 \rangle - \frac{1}{2} \rho_0 \langle |\mathbf{u}_1|^2 \rangle \tag{8}$$

where $\kappa_0 = \frac{1}{\rho_0 c_0^2}$ is the fluid compressibility. Eq. 8 illustrates that the second-order pressure need not vanish, in general, after time averaging, as it is involves products of first-order fields. These terms can thus furnish acoustic pressure with non-zero time average, and thus can elicit low-frequency shear wave oscillations that can be felt by the skin (*33–36*). Neglecting viscous forces, which can be shown to be small, the acoustic radiation pressure may be expressed in

terms of field quantities expanded up to second-order

$$\mathbf{F}_L = \iint_{S'} dS' \Big(- \big[\frac{1}{2}\kappa_0 \langle p_1^2 \rangle - \frac{\rho_0}{2} \langle |\mathbf{u}_1|^2 \rangle\big] \mathbf{I} - \rho_0 \langle \mathbf{u}_1 \otimes \mathbf{u}_1 \rangle \Big) \cdot \mathbf{n} \tag{9}$$

Elastic Wave Simulation Details

Elastic wave simulations were performed using the k-Wave Matlab toolbox (*37*). The simulations employ a Kelvin-Voigt model of viscoelasticity. While other models, such as the standard linear solid (SLS) and fractional Kelvin-Voigt models, have been found to more closely match the rheological properties of human tissue and similar materials (such as synthetic polymers) (*39*), the *k*-space pseudospectral method we employed facilitated efficient testing of many different air-coupled ultrasound scanning patterns with high temporal and spatial resolution. The results were consistent with those we obtained in our laboratory experiments (see Movies S1 and S2).

The simulated computational domain consisted of a 25 cm diameter and 1 cm thickness cylindrical, tissue-like material (mass density: 923.5 kg/m^3) placed upon a simulated square steel plate (25 cm edge length, mass density 8050 kg/m^3). The medium was surrounded on three sides by an air-like material (mass density: 100 kg/m^3). The computational domain was bounded by perfectly matched layers that absorbed energy, simulating open-boundary conditions, thus appropriately emulating free-space radiation conditions. The large difference in acoustic impedance between the tissue and the air and steel media implied that minimal energy was transmitted from the tissue into those media, while the substantial absorption in the non-tissue media also caused the energy of oscillations in those domains to be greatly attenuated (absorption: 300,000 dB/MHz^2 cm). Simulated tissue parameters approximately matched those of the measured specimen in the frequency regime of interest (absorption: 300,000 dB/MHz^2 cm; shear wave speed: 5 m/s), and the same attributes aided simulation convergence. Compres-

sion waves are negligible in the regime of interest, facilitating efficient and stable simulation with a moderate time step size (≈ 5 μs) and permitting simulations on the order of 100 ms. Shear wave components in non-tissue media could be neglected. We confirmed that the simulations results were stable with respect to changes in attributes of the non-tissue media.

In the simulations, we employed the same spatiotemporal modulation display technique we used in the laboratory experiments. The scanned ultrasound source had a Gaussian focal profile and a full width at half maximum (FWHM) of $\sim$0.6 cm across the top surface of our tissue-like material. The source intensity was held constant, apart from a short ($<$1 ms) ramp-in and ramp-out phase at the beginning and end of the scanning path. We tested and report data from a number of different source paths in our work including lines (Fig. 1), zig-zag patterns (Fig. 1C), squares (Fig. 3), and circles (Fig. 4, Fig. S1). For the circular and square scanning trajectories, the closed path was traversed multiple (two to six) times in a single trial. A steady-state wave field pattern was observed with as few as two traversals. A further experiment investigated how the rate at which the focus location was updated (focus control rate) affected shear shock front formation (Fig. 2). In this experiment, we updated the focused ultrasound source location at rates (0.7, 1.4, and 4.2 kHz) that were far below the simulation sample rate (200 kHz) with scanning speed held constant. Qualitatively similar shock wave patterns were formed in all conditions.

Wave Focusing: Figures of Merit

We evaluated wave focusing quality using metrics that have often been applied to analogous problems. We measured the mean-squared error (MSE) between discretized scalar fields (here, normal shear wave energy densities) x_{ij}, y_{ij}, where i and j index computing or measurement

grid coordinates on the surface of the medium:

$$MSE(x,y) = \frac{1}{MN}\sum_{i=1}^{M}\sum_{j=1}^{N}(x_{ij} - y_{ij})^2 \tag{10}$$

We also computed the structural similarity index (SSIM), which is a widely-used similarity measure that accommodates differences in spatial arrangement of otherwise similar scalar fields (*40*). It is given by:

$$SSIM(x,y) = l(x,y)^{\alpha}c(x,y)^{\beta}s(x,y)^{\gamma} \tag{11}$$

where α, β, and γ are parameters that were set to the simplest values of 1 for our computations, as is commonplace. Here, $l(x,y)$, $c(x,y)$, and $s(x,y)$ are luminance, contrast, and structural terms, defined by:

$$l(x,y) = \frac{2\mu_x\mu_y + C_1}{\mu_x^2 + \mu_y^2 + C_1} \tag{12}$$

$$c(x,y) = \frac{2\sigma_x\sigma_y + C_2}{\sigma_x^2 + \sigma_y^2 + C_2} \tag{13}$$

$$s(x,y) = \frac{2\sigma_{xy} + C_3}{\sigma_x\sigma_y + C_3} \tag{14}$$

where $\mu_x, \mu_y, \sigma_x, \sigma_y$, and σ_{xy} are the means, standard deviations, and cross-covariance of scalar fields x, y and C_1, C_2, and C_3 are regularization constants. The value of the SSIM metric ranges from 0 to 1, with 1 indicating perfect correspondence.

We analyzed wave field focusing quality by computing the energy density at each of the computational grid locations for the entire length of the simulation (which varied depending on the transverse speed of the stimulus):

$$E_{rms}(\mathbf{x}) = \frac{1}{2}\rho v_{rms}(\mathbf{x})^2 \tag{15}$$

where ρ was the mass density of the simulated medium (set to 923.47 kg/m^3 for all simulations). We used this quantity to compute the focus energy ratio (FER), r_E, as the ratio of the average

RMS energy density in the focus region to the average residual energy outside the path of the stimulus. We associated the focus region with the FWHM of an equivalent Gaussian field.

$$r_E = \frac{\frac{1}{N}\sum_{n=1}^{N} E_{rms}(\mathbf{x}_n)}{\frac{1}{M}\sum_{m=1}^{M} E_{rms}(\mathbf{y}_m)} \,, \tag{16}$$

where $\mathbf{x}_n$ and $\mathbf{y}_m$ are measurement or simulation locations inside and outside the source focal path, respectively. While we identified these measures to be most appropriate, we also performed further analyses (not shown here) using other common measures of focus quality, such as the contrast ratio, a measurement of energy confinement near the focus (*41*), and the focus area, the area of the contour on the medium surface for which the wave field energy attenuated by one-half (*42*). The findings were consistent with those we obtained using the metrics reported in the main manuscript, as described in the present section.

Vibrometry Measurements with Elastomer Plate

Elastomer Plate Construction

We constructed a cylindrical soft elastomer plate with diameter 28 cm and thickness 1 cm. The plate was molded from synthetic medical gelatin (Gelatin #2, Humimic, USA, mass density: 923.47 kg/m^3). We constructed the mold via laser cutting, machining, and stacking polycarbonate layers. We sprayed the mold with a releasing agent and coated the inverse top of the mold with reflective glass microbeads, which allowed us to use optical vibrometry to measure surface vibrations. The elastomer was placed in the mold, melted in a laboratory oven at 95°C, and allowed to cool at ambient temperature. The elastomer was then demolded and positioned on a polycarbonate base; the base was clamped to an optical table.

Apparatus

We measured surface vibrations at more than 1200 locations on the elastomer via scanning laser doppler vibrometer (Ometron, model 8330). Measurement points were distributed on a 5 mm spatial grid. The vibrometer was positioned 70 cm above the elastomer, inclined an angle of 45°. The scanning laser was controlled using custom software. A digital-to-analog converter (National Instruments Model 6321, USA, 16 bits, sample rate 10 kHz) delivered signals that controlled the position of the laser on the elastomer. An analog-to-digital converter (National Instruments Model 6321, USA, 16 bits, sample rate 48 kHz) captured the data. An ultrasound phased array (UHEV1, Ultrahaptics, Ltd.) stimulated the elastomer via focal points that scanned trajectories along the surface of the medium at specified speeds. The ultrasound device was positioned above the center of the elastomer at a height of 15 cm, which ensured that the device did not occlude the vibrometer (Fig. 5A). To minimize influence of ancillary acoustic reflections, we captured measurements from a circular surface domain of the elastomer of diameter 21 cm (Fig. 5B).

At the slowest stimulus scanning speeds ($v < 4$ m/s) we captured at least 20 measurements of all points on the elastomer surface, ensuring high signal-to-noise ratio. This required approximately 3 hours per stimulus scanning configuration. For the fast speeds ($v \geq 4$ m/s) each stimulus was repeated 8 times. This took approximately 1 hour per configuration. A trigger signal from the ultrasound array electronics ensured accurate measurement synchronization, thus furnishing temporally- and spatially-resolved wave field measurements on the surface of the elastomer, when elicited by the moving ultrasound focal points.

Human Hand Measurements

We analyzed vibrometry data that were previously captured as the right hand of three human participants was stimulated via focused ultrasound. A complete dataset was captured from one participant (age 24, male), furnishing the primary data analyzed in this manuscript. Partial datasets captured from the remaining two (ages 24, and 27, both male) were used in order to validate the larger dataset. The results were similar across all hands. At the time of data collection, written, informed consent was gathered from all participants and the experiment was conducted according to the protocol approved by the human subjects committee of our institution (University of California, Santa Barbara Human Subjects Committee).

Skin vibrations were captured normal to the volar surface of the hand using a scanning laser doppler vibrometer (PSV-500, Polytec, Inc., sample rate 125 kHz). The vibrometer was placed directly above the participant's hand at a height of 30 cm. The participant's hand was fixed to a vibration-isolated table using 3D printed brackets. The brackets were anchored to the table and attached to the participant's fingernails via double-sided adhesive. Participants reclined at a height that enabled the arm to be relaxed throughout the measurements. The ultrasound phased array (UHEV1, Ultrahaptics, Ltd.) was configured so that it did not occlude the SLDV (Fig. 5C). We compensated for the modest angle of incidence in software. Five different scanning speeds were used ($v_l = 1, 2, 4, 7, 11$ m/s). The motion path extended from the proximal base of the thenar eminence to the distal end of digit 2 or vice-versa, was registered to the anatomy of the hand, and was approximately 16 cm long. Synchronous data capture was ensured via a hardware trigger signal from the ultrasound device. The 300 measurements points were captured on a uniform grid. For each of the 5 speeds and 2 directions, we captured two complete 300-point spatiotemporal scans.

The data consisted of recorded skin velocity normal to the volar hand surface for each of

300 measurement points, $\mathrm{u}(\mathbf{x}, t)$. We removed a small minority of outlier measurement points for which signal-to-noise ratio was low. To generate the figures, we applied a spatial mean filter leveraging the position data captured from the integrated geometry scanner of SLDV, interpolated using the natural neighbor method, and applied a Gaussian low-pass reconstruction filter. We computed the wake length along the motion axis as follows: for each frame, we projected all hand data onto the axis defined by the index finger, binned the projected data using the maximum value over a small interval (1 pixel/ 0.27 mm), and determined the number of bins for which the magnitude of vibration velocity was greater than 10% of the maximum vibration velocity measured for that frame. We computed this measure of spatial extent across all time-frames for which the focus was well-defined on the palm of the hand (maximum vibration velocity at frame i was greater than 75% of the maximum vibration velocity for the entire stimulus duration, $\max_x |\mathrm{u}(\mathbf{x}, t_i)| > 0.75 \max_{\{\mathbf{x},t\}} |\mathrm{u}(\mathbf{x}, t)|$).

Tactile Motion Perception

We analyzed data from a previous experiment on tactile motion perception using stimulation conditions matching those in the human hand vibrometry experiment. There were twelve participants in total (ages 19-28, 6 female and 6 male), none of which reported any abnormality in touch sensation. Written, informed consent was gathered for all participants at the time the data was collected, and the experiment was conducted according to the protocol approved by the human subjects committee of our institution (University of California, Santa Barbara Human Subjects Committee).

The apparatus was similar to the one used in the hand measurements. Each participant was seated with their right hand resting on a foam surface and the forearm supported by an armrest. The ultrasound display was positioned 15 cm above the volar hand surface. The hand was fixated via a support surface adhered at sparse locations on the dorsal hand surface.

Stimulus conditions matched those used in the vibrometry experiment, with the addition of a lower scanning speed condition ($v_l = 0.5$). Participants wore earplugs (attenuation rating 33 dB) and circumaural headphones which played pink noise. During each trial, they judged the motion direction of the stimulus, which could be played as many times as participants preferred. Stimuli were block randomized. Each block was repeated 10 times; participant completed 120 trials (6 speeds, 2 directions, and 10 repetitions). Responses were collected via a desktop computer. The binary response data were analyzed using a Generalized Linear Mixed Model (GLMM). We used a logistic link function, $y = \log(\frac{\mu}{1-\mu})$, where μ was the proportion of correct responses, in our model specification to interpret our binary response data. "Direction" and "Speed" (and their interaction) were treated as fixed effects, while "Participant" was treated as a random effect.

In the primary behavioral experiment (described above and in the main text), scanning trajectories traversed the entire length of the hand with different scanning speeds, which could raise concerns about the confounding effects of duration on the results. To confirm that the conclusions drawn from this study were not affected by variations in duration, we designed and conducted an additional study in which duration was held nearly constant. We achieved this by cyclically repeating each stimulus along the scanning path in a manner that depended on the stimulus speed v. The number N of repetitions was selected such that the total duration $T = N\tau(v)$ was approximately constant as the duration $\tau(v)$ of the stimuli varied. We conducted two versions of this experiment: one in which the repeated traversal of the motion path occurred without delay, and another in which the repeated traversal of the motion path occurred after a time delay (500 ms) that ensured skin oscillations attenuated before the next repetition, avoiding overlap between the stimuli. Other conditions were identical to those used in the primary behavioral experiment. Three participants completed each version of the experiment, and each gave their written, informed consent. The results were very similar to our

findings from the main experiment. Motion perception accuracy was high at low speeds and dropped to chance levels for the highest speeds (Fig. S3A). Comparable results were obtained in both experiments, with and without the 500 ms time delay, although the limited size of this confirmatory study precludes meaningful statistical analysis. The similarity of these findings with those from our primary experiment may reflect the fact that these findings are conserved when the stimulus duration varied. The similarity may also reflect that (as noted in the main text) participants in the primary experiment elected to replay higher-speed stimuli more often (Fig. S3B), partly compensating for differences between stimulus duration.

We also evaluated other variations on our tactile motion perception experimental design, including one, for which pilot results are presented here, in which circular scanning trajectories were used. The circular trajectories (radius 2.8 cm) were drawn on the palm of the hand in clockwise and counter-clockwise directions and duration was held constant using the same method as described above. Other conditions were identical to those used in the main experiment. Results from the one participant who completed this pilot study, after supplying his written, informed consent, are shown in Fig. S3C. Perceptual accuracy was near chance levels at all speeds. The participant verbally reported the motion direction to be very difficult to perceive. Others who tried the stimuli without completing the entire experiment also found the motion direction very difficult to perceive. These observations appear to be consistent with results from our vibrometry experiments with circular trajectories (Fig. 4, Fig. S1) that demonstrate the complex relationship between skin oscillation patterns and the speed of scanning along circular trajectories.

Supplementary Figures

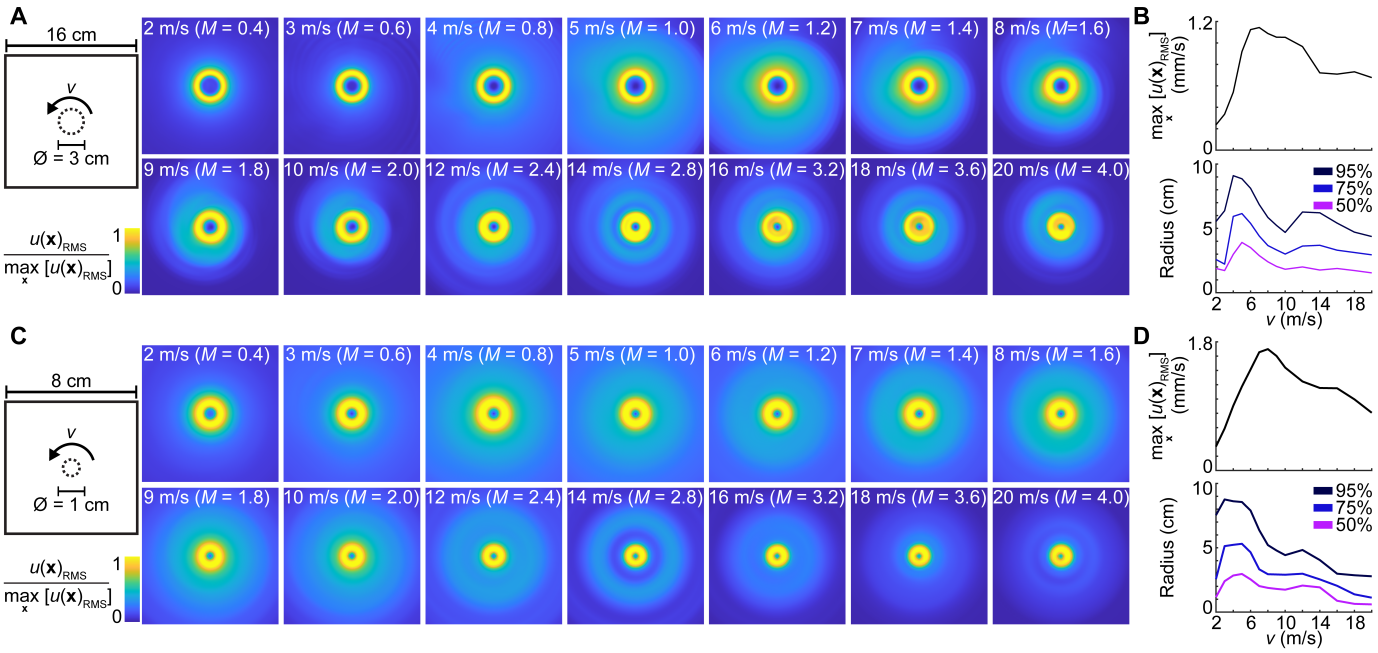

Fig. S1: Shear shock wave formation in numerically simulated tissue during scanning along closed circular trajectories with different diameters. (**A,C**) Time-averaged wave fields for different scanning speeds, v (normalized RMS oscillation velocity shown). (**B,D**) Maximum RMS oscillation velocity (top panel) and radius which contains 50%, 75%, and 95% of the total wave field energy (bottom panel) as a function of the scanning speed, v . Constructive interference of wavefronts in the region circumscribed by the scanning trajectory produced the greatest wave amplitude along a smaller circle whose radius was greatest at approximately $M = 1$ and then decreased substantially as M increased into the supersonic regime.

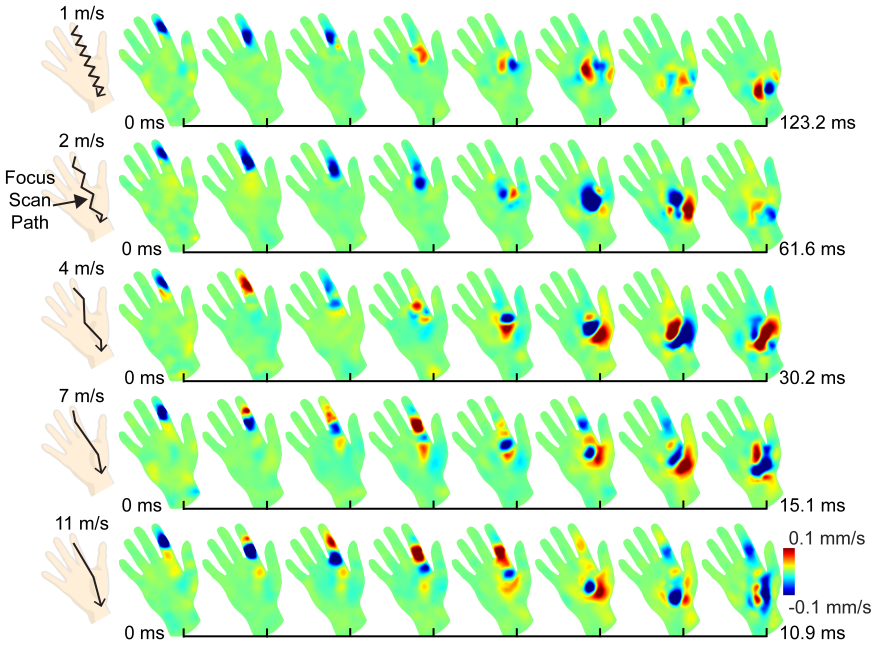

Fig. S2: High-speed scanning of a focused ultrasound source produces trailing wakes on the volar hand surface. *In vivo* viscoelastic wave patterns, revealed via optical vibrometry, as the ultrasound focus scanned from the distal end of digit 2 to the wrist (oscillation velocity, $u(\mathbf{x}, t)$, shown). High scanning speeds produced wake patterns which trailed up to 10 cm behind the focus.

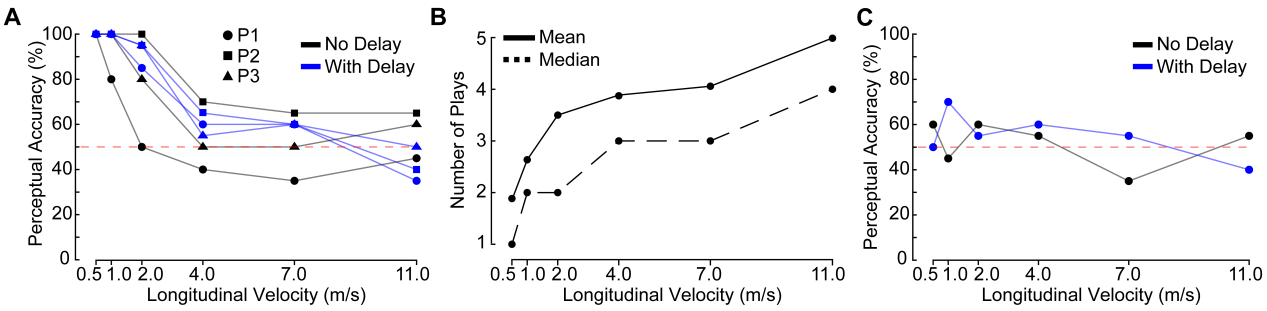

Fig. S3: Extended results: tactile motion experiments with duration held approximately constant. (**A**) Mean perceptual accuracy vs. scanning speed, with other conditions identical to those used in the main experiment (3 participants: P1, P2, and P3). (**B**) Results from the main experiment: number of repetitions of stimuli at each speed. Participants elected to repeat shorter stimuli more times thus reducing differences between total time that stimuli were felt at each speed. (**C**) Results from pilot study ($N = 1$) using constant-duration circular trajectories (radius 2.8 cm) drawn on the palm at different scanning speeds, rather than linear trajectories as were used in the primary experiment. Perceptual accuracy was near chance levels at all speeds.

Movie S1: Comparison between simulated and measured response on a tissue phantom to a *subsonic* moving focused ultrasound source (v = 4 m/s).

Movie S2: Comparison between simulated and measured response on a tissue phantom to a *supersonic* moving focused ultrasound source (v = 7 m/s).

Movie S3: Comparison between measured vibration responses on a tissue phantom to a subsonic and supersonic focused ultrasound source scanned along a zig-zag path.

REFERENCES AND NOTES

1. T. Hoshi, M. Takahashi, T. Iwamoto, H. Shinoda, Noncontact tactile display based on radiation pressure of airborne ultrasound. *IEEE Trans. Haptics* **3**, 155–165 (2010).

2. T. Carter, S. A. Seah, B. Long, B. Drinkwater, S. Subramanian, Ultrahaptics: Multi-point mid-air haptic feedback for touch surfaces, in *Proceedings of the 26th Annual ACM Symposium on User Interface Software and Technology* (ACM, 2013), pp. 505–514.

3. A. Marzo, B. W. Drinkwater, Holographic acoustic tweezers. *Proc. Natl. Acad. Sci. U.S.A.* **116**, 84–89 (2019).

4. B. Long, S. A. Seah, T. Carter, S. Subramanian, Rendering volumetric haptic shapes in mid-air using ultrasound. *ACM Transactions on Graphics (TOG)* **33**, 1–10 (2014).

5. G. Wilson, T. Carter, S. Subramanian, S. A. Brewster, Perception of ultrasonic haptic feedback on the hand: Localisation and apparent motion, in *Proceedings of the 32nd Annual ACM Conference on Human Factors in Computing Systems* (ACM, 2014), pp. 1133–1142.

6. H. Barreiro, S. Sinclair, M. A. Otaduy, Path routing optimization for STM ultrasound rendering. *IEEE Trans. Haptics* **13**, 45–51 (2020).

7. O. Georgiou, C. Jeffrey, Z. Chen, B. X. Tong, S. H. Chan, B. Yang, A. Harwood, T. Carter, Touchless haptic feedback for VR rhythm games, in *2018 IEEE Conference on Virtual Reality and 3D User Interfaces (VR)* (IEEE, 2018), pp. 553–554.

8. E. Freeman, R. Anderson, J. Williamson, G. Wilson, S. A. Brewster, Textured surfaces for ultrasound haptic displays, in *Proceedings of the 19th ACM International Conference on Multimodal Interaction* (2017), pp. 491–492.

9. I. Rakkolainen, E. Freeman, A. Sand, R. Raisamo, S. Brewster, A survey of mid-air ultrasound haptics and its applications. *IEEE Trans. Haptics* **14**, 2–19 (2021).

10. M. Obrist, S. A. Seah, S. Subramanian, Talking about tactile experiences, in *Proceedings of the SIGCHI Conference on Human Factors in Computing Systems* (ACM, 2013), pp. 1659–1668.

11. T. Iwamoto, D. Akaho, H. Shinoda, High resolution tactile display using acoustic radiation pressure, in *SICE 2004 Annual Conference* (IEEE, 2004), vol. 2, pp. 1239–1244.

12. K. Hasegawa, H. Shinoda, Aerial display of vibrotactile sensation with high spatial-temporal resolution using large-aperture airborne ultrasound phased array, in *2013 World Haptics Conference (WHC)*, Daejeon, Korea (South), 14 to 17 April 2013 (IEEE, 2013), pp. 31–36.

13. S. Inoue, Y. Makino, H. Shinoda, Active touch perception produced by airborne ultrasonic haptic hologram, in *2015 IEEE World Haptics Conference (WHC)*, Evanston, IL, USA, 2015 (IEEE, 2015), pp. 362–367.

14. G. Reardon, Y. Shao, B. Dandu, W. Frier, B. Long, O. Georgiou, Y. Visell, Cutaneous wave propagation shapes tactile motion: Evidence from air-coupled ultrasound, in *2019 IEEE World Haptics Conference (WHC)*, Tokyo, Japan, 9 to 12 July 2019 (IEEE, 2019), pp. 628–633.

15. J. Chilles, W. Frier, A. Abdouni, M. Giordano, O. Georgiou, Laser doppler vibrometry and FEM simulations of ultrasonic mid-air haptics, in *2019 IEEE World Haptics Conference (WHC)*, Tokyo, Japan, 9 to 12 July 2019 (IEEE, 2019), pp. 259–264.

16. W. Frier, A. Abdouni, D. Pittera, O. Georgiou, R. Malkin, Simulating airborne ultrasound vibrations in human skin for haptic applications. *IEEE Access* **10**, 15443–15456 (2022).

17. W. Frier, D. Ablart, J. Chilles, B. Long, M. Giordano, M. Obrist, S. Subramanian, Using spatiotemporal modulation to draw tactile patterns in mid-air, in *International Conference on Human Haptic Sensing and Touch Enabled Computer Applications* (Springer, 2018), pp. 270–281.

18. R. Takahashi, K. Hasegawa, H. Shinoda, Tactile stimulation by repetitive lateral movement of midair ultrasound focus. *IEEE Transac. Haptics* **13**, 334–342 (2019).

19. K. O. Johnson, The roles and functions of cutaneous mechanoreceptors. *Curr. Opin. Neurobiol.* **11**, 455–461 (2001).

20. R. S. Johansson, U. Landström, R. LLundström, Sensitivity to edges of mechanoreceptive afferent units innervating the glabrous skin of the human head. *Brain Res.* **244**, 27–35 (1982).

21. W. Frier, D. Pittera, D. Ablart, M. Obrist, S. Subramanian, Sampling strategy for ultrasonic mid-air haptics, in *Proceedings of the 2019 CHI Conference on Human Factors in Computing Systems* (2019), pp. 1–11.

22. L. R. Manfredi, A. T. Baker, D. O. Elias, J. F. Dammann, M. C. Zielinski, V. S. Polashock, S. J. Bensmaia, The effect of surface wave propagation on neural responses to vibration in primate glabrous skin. *PLOS ONE* **7**, e31203 (2012).

23. A. E. Knight, A. B. Pely, F. Q. Jin, A. R. Cardones, M. L. Palmeri, K. R. Nightingale, Analysis of factors affecting shear wave speed in in vivo skin, in *2019 IEEE International Ultrasonics Symposium (IUS*) (IEEE, 2019), pp. 970–973.

24. T. J. Moore, A survey of the mechanical characteristics of skin and tissue in response to vibratory stimulation. *IEEE Trans. Hum Mach. Syst.* **11**, 79–84 (1970).

25. J. Bercoff, M. Tanter, M. Fink, Supersonic shear imaging: A new technique for soft tissue elasticity mapping. *IEEE Trans. Ultrason. Ferroelectr. Freq. Control* **51**, 396–409 (2004).

26. S. Alekseenko, A. Cherep, Spiral waves in dispersive media. *Acta Mech.* **105**, 143–160 (1994).

27. L. A. Jones, S. J. Lederman, *Human Hand Function* (Oxford Univ. Press, 2006).

28. S. Holm, *Waves With Power-Law Attenuation* (Springer Cham, Springer Nature Switzerland, 2019).

29. J. H. Kaas, Somatosensory system, in *The Human Nervous System* (Academic Press, 2004), pp. 1059–1092.

30. Y. Shao, V. Hayward, Y. Visell, Spatial patterns of cutaneous vibration during whole-hand haptic interactions. *Proc. Natl. Acad. Sci. U.S.A.* **113**, 4188–4193 (2016).

31. Y. Shao, H. Hu, Y. Visell, A wearable tactile sensor array for large area remote vibration sensing in the hand. *IEEE Sens. J.* **20**, 6612–6623 (2020).

32. Y. Shao, V. Hayward, Y. Visell, Compression of dynamic tactile information in the human hand. *Sci. Adv.* **6**, eaaz1158 (2020).

33. T. Hasegawa, T. Kido, T. Iizuka, C. Matsuoka, A general theory of rayleigh and langevin radiation pressures. *Acoust. Sci. Technol.* **21**, 145–152 (2000).

34. A. Doinikov, Acoustic radiation pressure on a rigid sphere in a viscous fluid. *Proc. R. Soc. Lond. A Math. Phys. Sci.* **447**, 447–466 (1994).

35. S. Danilov, M. Mironov, Mean force on a small sphere in a sound field in a viscous fluid. *J. Acoust. Soc. Am.* **107**, 143–153 (2000).

36. M. Settnes, H. Bruus, Forces acting on a small particle in an acoustical field in a viscous fluid. *Phys. Rev. E* **85**, 016327 (2012).

37. B. E. Treeby, J. Jaros, D. Rohrbach, B. Cox, Modelling elastic wave propagation using the k-wave matlab toolbox, in *2014 IEEE International Ultrasonics Symposium* (IEEE, 2014), pp. 146–149.

38. J. Friend, L. Y. Yeo, Microscale acoustofluidics: Microfluidics driven via acoustics and ultrasonics. *Rev. Mod. Phys.* **83**, 647–704 (2011).

39. S. P. Kearney, A. Khan, Z. Dai, T. J. Royston, Dynamic viscoelastic models of human skin using optical elastography. *Phys. Med. Biol.* **60**, 6975 (2015).

40. Z. Wang, A. C. Bovik, H. R. Sheikh, E. P. Simoncelli, Image quality assessment: From error visibility to structural similarity. *IEEE Trans. Image Process.* **13**, 600–612 (2004).

41. C. Hudin, J. Lozada, V. Hayward, Spatial, temporal, and thermal contributions to focusing contrast by time reversal in a cavity. *J. Sound Vib.* **333**, 1818–1832 (2014).

42. G. Reardon, N. Kastor, Y. Shao, Y. Visell, Elastowave: Localized tactile feedback in a soft haptic interface via focused elastic waves, in *2020 IEEE Haptics Symposium (HAPTICS)* (IEEE, 2020), pp. 7–14.